Anomalous localization in non-Hermitian sonic lattice with erratic skin modes

Chengwu Ji(季成武), Guofeng Yang(杨国锋), Bolun Hu(胡博伦)
Citation: Chin. Phys. B. 35, 104301 (2026). DOI: 10.1088/1674-1056/ae2a03 | CSTR: 32038.14.CPB.ae2a03
http://cpb.iphy.ac.cn; http://iopscience.iop.org/cpb

What follows is a list of articles you may be interested in

Boundary effects on modal shape in deep ocean via non-integer order parabolic cylinder functions

Jian-Kang Zhan(詹建康), Sheng-Chun Piao(朴胜春), Li-Jia Gong(龚李佳)
Chin. Phys. B. 35, 024303 (2026). DOI: 10.1088/1674-1056/ae1b7c | CSTR: 32038.14.CPB.ae1b7c

Ultrasonic scalpel based on fusiform phononic crystal structure

Sha Wang(王莎), Junjie Shan(单俊杰), Shuyu Lin(林书玉)
Chin. Phys. B. 33, 104302 (2024). DOI: 10.1088/1674-1056/ad6a0c

Inverse design of nonlinear phononic crystal configurations based on multi-label classification learning neural networks

Kunqi Huang(黄坤琦), Yiran Lin(林懿然), Yun Lai(赖耘), Xiaozhou Liu(刘晓宙)
Chin. Phys. B. 33, 104301 (2024). DOI: 10.1088/1674-1056/ad6b85

Non-Kramers doublet ground state in a quaternary cubic compound $PrRu_2In_2Zn_{18}$ investigated by ultrasonic measurements

Hua-Yuan Zhang(张化远), Kazuhei Wakiya, Mitsuteru Nakamura, Masahito Yoshizawa, Yoshiki Nakanish
Chin. Phys. B. 33, 064301 (2024). DOI: 10.1088/1674-1056/ad35af

Sensing the heavy water concentration in an H_2O–D_2O mixture by solid–solid phononic crystals

Mohammadreza Rahimi, Ali Bahrami
Chin. Phys. B. 33, 044301 (2024). DOI: 10.1088/1674-1056/ad0bf5

Anomalous localization in non-Hermitian sonic lattice with erratic skin modes

Chengwu Ji(季成武), Guofeng Yang(杨国锋)[†], and Bolun Hu(胡博伦)[‡]

School of Optoelectronic Information and Physical Science, Jiangnan University, Wuxi 214122, *China*

(Received 1 November 2025; revised manuscript received 3 December 2025; accepted manuscript online 9 December 2025)

Controlling the sound field in non-Hermitian acoustic systems remains a fundamental challenge with implications for energy harvesting and sensing. In this work, we present the first comprehensive numerical simulation and characterization of the erratic non-Hermitian skin effect (ENHSE) in a disordered sonic lattice. Unlike the conventional non-Hermitian skin effect that confines waves to the boundaries, the ENHSE generates random, irregular wave localization patterns that can emerge anywhere in the system — either at edges or in the bulk. Our full-wave simulations reveal a significant correlation between localization patterns under periodic boundary conditions (PBC) and open boundary conditions (OBC): the positions of primary localization centers remain consistent, while a subset of sharp peaks observed under PBC transform into valleys under OBC, flanked by secondary peaks on both sides. Furthermore, we demonstrate that by tailoring coupling strengths to locally engineer the imaginary gauge field, precise control over the localized fields can be achieved. This novel approach of wave energy localization establishes a practical new paradigm for wave manipulation in non-Hermitian systems, with direct applications to acoustic sensing, energy harvesting, and reconfigurable metamaterials.

Keywords: non-Hermitian skin effect (NHSE), sonic lattice, metamaterial

PACS: 43.20.+g, 03.65.Vf, 11.30.Er

DOI: 10.1088/1674-1056/ae2a03 **CSTR:** 32038.14.CPB.ae2a03

1. Introduction

Non-Hermitian physics, characterized by complex eigenvalues and non-orthogonal eigenstates, has emerged as a powerful framework for describing open and dissipative systems.[1–7] In classical wave systems, judicious introduction of gain and loss enables exotic phenomena with no Hermitian counterpart, including exceptional-point-based sensing,[8–10] parity-time-symmetric unidirectional transport,[11–17] and the non-Hermitian skin effect (NHSE).[18–23] The NHSE, manifested as exponential accumulation of bulk eigenstates at system boundaries under open boundary conditions (OBC),[23–27,29] represents a particularly striking departure from conventional wave behavior and has attracted intense research interest for its implications in wave localization and topological physics.[28–32,35]

The NHSE, wherein all eigenstates — both bulk and boundary modes — accumulate at specific boundaries, originates from the fundamental disparity between periodic boundary conditions (PBC) and OBC when non-reciprocal coupling is introduced into the system. Under PBC, the system supports extended Bloch-like states, whereas under OBC, all eigenstates collapse toward boundaries with their spatial distribution determined by the specific non-reciprocal coupling configuration.[33–35] However, previous studies have primarily focused on uniform or deterministic non-reciprocal coupling patterns, resulting in predictable, boundary-localized modes that offer limited spatial control and programmability. A fundamental question arises: Can disorder in non-reciprocal coupling — rather than being detrimental — be harnessed to achieve controllable wave localization beyond system boundaries?

Here, we introduce a different approach by incorporating disordered non-reciprocal couplings in a one-dimensional Hatano–Nelson sonic lattice. This design gives rise to an erratic non-Hermitian skin effect (ENHSE) — a regime where eigenstates localize at irregular positions throughout the system.[36] In extended lattices, we find that the sound field under OBC exhibits a localization pattern strongly correlated with the PBC case. The primary localization centers remain unchanged, yet for a subset of the sharp peaks observed under PBC, the profile collapses into a valley, flanked by two secondary peaks. Finally, we demonstrate precise engineering of the localization pattern in a finite sonic lattice by designing the gauge field sequence. Introducing localized parameter defects confirms the robustness of the construct and leads to enhanced localization properties. Our results establish disorder-engineered non-Hermitian systems as a programmable platform for acoustic energy concentration, and compact acoustic devices.

2. Model and the emergent erratic non-Hermitian skin effect

To elucidate this novel phenomenon, we construct a sonic system based on the Hatano–Nelson (HN) model. As shown

[†]Corresponding author. E-mail: gfyang@jiangnan.edu.cn

[‡]Corresponding author. E-mail: hubolun@jiangnan.edu.cn

© 2026 Chinese Physical Society and IOP Publishing Ltd. All rights, including for text and data mining, AI training, and similar technologies, are reserved.

in Fig. 1(a), both the conceptual schematic (left panel) and the detailed structural layout of the non-Hermitian sonic lattice (right panel) depict a regular polygon with N sides. This specific geometry ensures uniform real coupling strengths throughout the system, which is essential for precise control of the effective couplings via gain-loss structures. While the arrangement resembles an SSH-like chain in appearance, it incorporates crucial distinctions that enable the observed non-Hermitian phenomena. First, the coupling between adjacent sites is non-reciprocal, indicated by arrows of different colors representing direction-dependent coupling strengths. Second, even along the same direction, the coupling strength is not necessarily uniform. The specific configuration responsible for the emergent erratic non-Hermitian skin effect will be detailed later. For the PBC case, non-reciprocal coupling also exists between the first and the last sites; whereas for OBC, the head-to-tail coupling is absent.

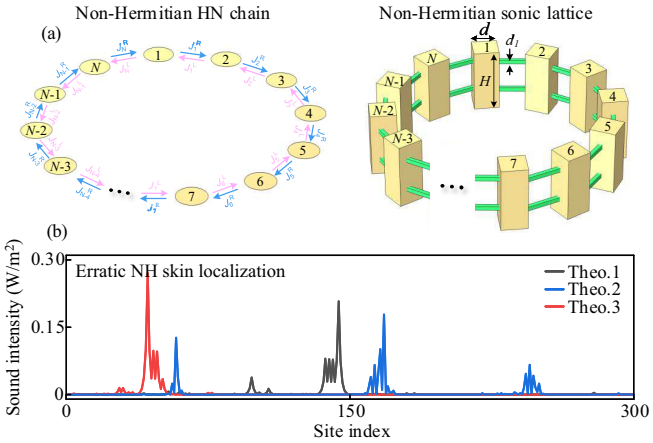

Fig. 1. Schematic of the non-reciprocal system and the resulting ENHSE. (a) Non-Hermitian HN chain and corresponding sonic lattice under PBC with disordered non-reciprocal couplings. The coupling from site n to $n+1$ is $J\exp(h_n)$, and from $n+1$ to n is $J\exp(-h_n)$, where the sequence $\{h_n\}$ is drawn from a Bernoulli distribution. (b) Characteristic spatial profiles of the acoustic energy in the ENHSE. Three representative eigenstates are depicted through their sound intensity distributions, each highly localized at distinct, random sites of the lattice.

The system is generally described by the following non-Hermitian tight-binding Hamiltonian:

$$\widehat{H} = \sum_{n=1}^{N-1} \left(J_n^{\mathrm{R}} c_{n+1}^{\dagger} c_n + J_n^{\mathrm{L}} c_n^{\dagger} c_{n+1} \right) + \widehat{A}. \tag{1}$$

Here, N is the system size, $c_n^{\dagger}$ and c_n are the creation and annihilation operators on site n, and $J_n^{\mathrm{R,L}}$ denote the hopping amplitudes to the right (R) and to the left (L), respectively. The operator $\widehat{A}$ accounts for the boundary term: $\widehat{A} = 0$ for OBC, and $\widehat{A} = J_N^{\mathrm{R}} c_1^{\dagger} c_N + J_N^{\mathrm{L}} c_N^{\dagger} c_1$ for PBC.

We introduce a spatially disordered imaginary gauge field h_n by defining the hopping amplitudes as

$$J_n^{\mathrm{R}} = J\exp(h_n), \quad J_n^{\mathrm{L}} = J\exp(-h_n), \tag{2}$$

where J is a constant. A key quantity is then defined as follows:

$$X_n = \sum_{k=1}^{n-1} h_k. \tag{3}$$

The eigenstates ψ_n and their corresponding eigenvalues E satisfy the equation

$$E\psi_n = J_{n-1}^{\mathrm{R}} \psi_{n-1} + J_n^{\mathrm{L}} \psi_{n+1} + \widehat{A}\psi_n. \tag{4}$$

For a system under OBC, the eigenvalues and eigenstates are given by

$$E = 2J\cos(q), \quad \psi_n^{(a)} = \sin(nq_a)\exp(X_n), \tag{5}$$

with $q = \alpha\pi/(N+1)$, where $\alpha = 1,\ldots,N$ and $n = 1,\ldots,N$. Here, $q_a = a\pi/(N+1)$ denotes the value of q when $\alpha = a$. In this notation, $\psi_n^{(a)}$ denotes the n-th component of the a-th eigenstate.

For a system under PBC, they become

$$E = 2J\cos\left(q + i\overline{h}\right), \quad \psi_n^{(a)} = \exp\left(inq_a - n\overline{h}\right)\exp(X_n), \tag{6}$$

where $\overline{h} = (1/N)\sum_{k=1}^{N} h_k$ (see Appendix A for full derivation). A critical insight from Eqs. (5) and (6) is that the eigenvalue spectra of the PBC and OBC systems become nearly identical when the average gauge field $\overline{h} \approx 0$, which is the prerequisite for our study of the ENHSE.

We design a one-dimensional non-Hermitian sonic lattice [right panel of Fig. 1(a)], which is a physical realization of the Hatano–Nelson model schematized in the left panel of Fig. 1(a). The lattice consists of acoustic cavities — each of height $H = 80$ mm and width $d = 32$ mm — coupled via narrow tubes of height $d_1 = 5$ mm that emulate the inter-site hopping. From these dimensions, we extract a coupling coefficient of $\alpha = 7.718 \times 10^{-3}$. The system is governed by the Hamiltonian

$$\widehat{H}_N^{\mathrm{PBC}} = f_0\mathbb{I} + \alpha f_0 J \cdot \begin{bmatrix} 0 & \mathrm{e}^{-h_1} & \cdots & 0 & \mathrm{e}^{h_N} \\ \mathrm{e}^{h_1} & 0 & \cdots & 0 & 0 \\ 0 & \mathrm{e}^{h_2} & \cdots & 0 & 0 \\ \vdots & \vdots & \ddots & \vdots & \vdots \\ 0 & 0 & \cdots & 0 & \mathrm{e}^{-h_{N-1}} \\ \mathrm{e}^{-h_N} & 0 & \cdots & \mathrm{e}^{h_{N-1}} & 0 \end{bmatrix}. \tag{7}$$

Here, $f_0 = 2144.1$ Hz denotes the fundamental resonance eigenfrequency of a single cavity, and $\mathbb{I}$ is a $N \times N$ identity matrix.

The computed eigenvalue spectrum in the complex plane is shown in Fig. 2(a). As predicted by Eqs. (5) and (6), when the imaginary gauge field h_n follows a Bernoulli distribution ($\pm\Delta h$ with equal probability), the spectral averaging condition $\overline{h} \approx 0$ is satisfied, leading to nearly identical spectra for PBC and OBC. This spectral overlap suppresses the conventional non-Hermitian skin effect, providing a well-defined setting in which to observe the ENHSE.

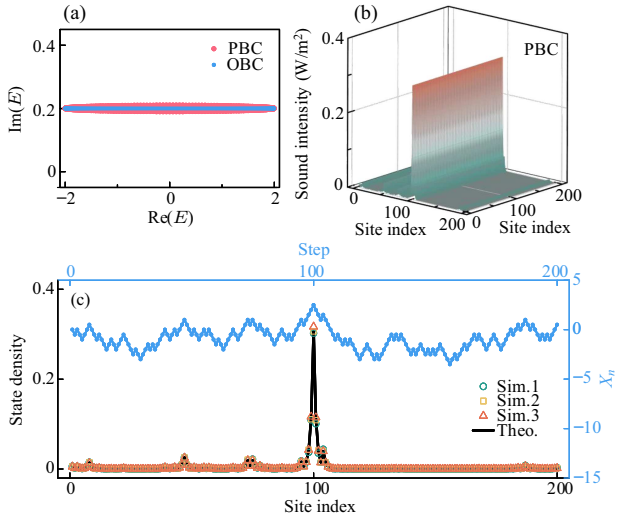

Fig. 2. Erratic eigenstates distribution in a non-Hermitian system under PBC. (a) Eigenvalue spectra for PBC (pink points) and OBC (blue points). (b) Theoretical spatial profile of the sound intensity. (c) A single plot combining two datasets: the spatial variation of X_n (refer to the right and top axes), indicating $\bar{h} \approx 0$ from the negligible net change across the lattice, is shown together with the simulated and theoretical spatial distributions of the sound intensity (refer to the left and bottom axes). The discrete points represent the sound intensity of three eigenstates from simulation, showing excellent agreement with the theoretical profile (black line). The localization centers align with the peaks in X_n. In (a)–(c), the system parameters are set to $N = 200$, $J = 1$, and $\Delta h = 0.5$.

Notably, all eigenstates of this PBC system share the same sound intensity profile (see Appendix A for detailed derivation). The theoretical distribution is plotted in Fig. 2(b). In Fig. 2(c), a cross section of this theoretical profile (referring to the left and bottom axes) is compared with the corresponding simulation results for three representative eigenstates. Close agreement is observed — both the positions and amplitudes of the main and satellite peaks match the theoretical prediction.

The sound intensity is concentrated at a small number of irregularly spaced sites, a hallmark of the ENHSE. We trace this localization pattern to the cumulative gauge parameter $X_n = \sum_{k=1}^{n-1} h_k$, whose spatial variation is simultaneously plotted in Fig. 2(c) (referring to the right and top axes). Crucially, the peaks in the spatial intensity distribution align precisely with the dominant peaks in X_n, specifically those with the largest amplitudes, indicating that localization is governed by the most extreme values in the accumulated disorder. Smaller features in X_n appear to have negligible effect. This correlation suggests a powerful design principle: by locally tailoring the elements of the sequence h_n to amplify selected local peaks in X_n, one can precisely engineer both the location and intensity of acoustic energy localization — a possibility we explore later.

3. Boundary effect and robust localization

A key finding is the dramatic difference in acoustic intensity distributions between PBC and OBC systems, which stems solely from the boundary conditions despite shared internal couplings. To clearly reveal these differences, we examine a lattice of size $N = 50$.

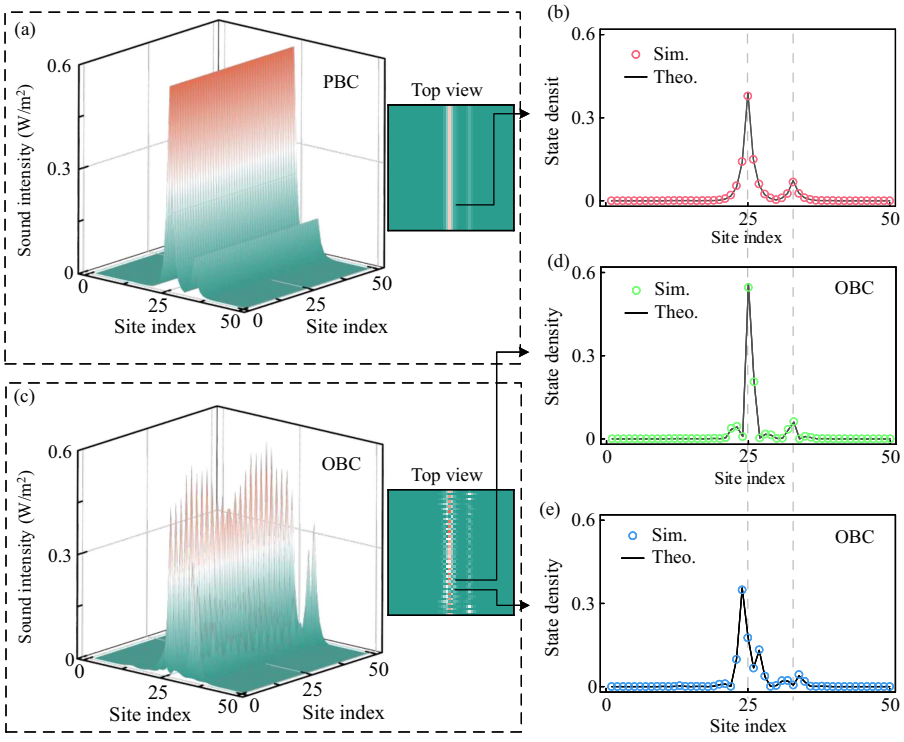

Fig. 3. Contrasting spatial distributions of sound intensity under periodic and open boundary conditions. (a), (b) PBC case: (a) Left: Theoretical 3D profile of the sound intensity; Right: The corresponding top view. (b) Comparison between the simulated intensity of a representative state (scatter points) and the theoretical profile (black line). (c)–(e) OBC case: (c) Theoretical 3D profile of the sound intensity presenting the top view alongside. (d), (e) Two characteristic patterns in the OBC intensity profiles: (d) A distribution featuring a primary and a satellite peak, structurally similar to the PBC case but with additional minor peaks. (e) A distribution where a subset of the primary and satellite peaks collapses, fragmenting into multiple peaks near the original localization centers. For all panels (a)–(e), the system parameters are $N = 50$, $J = 1$, and $\Delta h = 0.5$.

In the PBC system, the conventional NHSE is absent. Although all eigenvalues are distinct, their associated eigenstates share a single, identical spatial intensity profile, as visualized in the 3D plot of Fig. 3(a). Its top view shows this intensity profile consists of one dominant peak and one satellite peak of markedly different amplitude. The sound intensity distribution from a simulated eigenstate agrees closely with the theoretical prediction, as shown in Fig. 3(b).

The OBC system, in contrast, exhibits a more complex spatial intensity structure [Fig. 3(c)]. Ordering the states by increasing real part of their eigenvalues reveals a striking parity effect in the top view of the intensity distributions: among the first 25 states, the sound intensity of odd-numbered ones peaks at the central site ($n = 25$), while that of even-numbered ones exhibits a central valley flanked by two subsidiary peaks. This intensity pattern is symmetrically inverted for the latter 25 states, a consequence of the lattice's global reciprocity. Crucially, this parity-dependent modulation of the intensity profile applies not only to the main peak but also to the satellite peak, as confirmed by the theory-simulation comparisons in Figs. 3(d) and 3(e).

An analytical insight explains this phenomenon. From Eq. (5), the OBC eigenstates are $\psi_n^{(a)} = \sin(nq)\exp(X_n)$, with $q = a\pi/(N+1)$. The spatial intensity distribution, i.e., the sound intensity at site n for this state, is proportional to $\left|\psi_n^{(a)}\right|^2 = |\sin(nq)\exp(X_n)|^2$. At the lattice center ($n = N/2$), the factor $\exp(X_n)$ is common to all states. Thus, the intensity variation arises solely from the sinusoidal term, $|\sin(nq)|^2$. The intensity ratio between the a-th and the first state at the center is $\sin^2(a\beta)/\sin^2(\beta)$, where $\beta = N\pi/[2(N+1)]$. This relation directly yields the observed pattern, a zipper-like interlacing of intensity peaks and valleys across successive eigenstates.

Most importantly, Figs. 3(b), 3(d), and 3(e) demonstrate that the primary spatial localization centers in the intensity profiles are identical under both PBC and OBC. This highlights the robustness of the ENHSE: it presents as a static, uniform intensity profile for all states under PBC, and as a dynamic yet spatially fixed intensity pattern under OBC, where peak heights vary but the localization centers — dictated by the sequence h_n — remain unchanged.

4. Deterministic control of localization patterns

Having established that the localization is governed by the cumulative parameter X_n, we demonstrate precise control over the ENHSE by engineering the sequence h_n. To render the effects more pronounced, we analyze a finite-size lattice ($N = 19$) under PBC. Although a short lattice cannot perfectly realize a Bernoulli distribution, our theoretical framework identifies $\bar{h} \approx 0$ as the essential condition. We therefore manually construct sequences for h_1 to h_{19} that satisfy this requirement while being explicitly designed to yield targeted X_n profiles.

As shown in Figs. 4(a) and 4(b), we successfully implement sequences that produce X_n profiles with a single prominent peak and two prominent peaks, corresponding to symmetric and alternating gauge field configurations, respectively. The upper panels of Figs. 4(c) and 4(d) confirm that the spatial distribution of the acoustic field energy (proportional to $|p|^2$, p being the acoustic pressure) for a representative eigenstate reaches its maximum precisely at the predetermined sites dictated by the X_n peaks. The corresponding spatial intensity distributions, shown in the lower panels, exhibit close agreement between simulation and theory. These results collectively verify that the spatial profile of the ENHSE can be deterministically controlled through tailored design of the gauge field sequence, enabling the creation of localization sites at will.

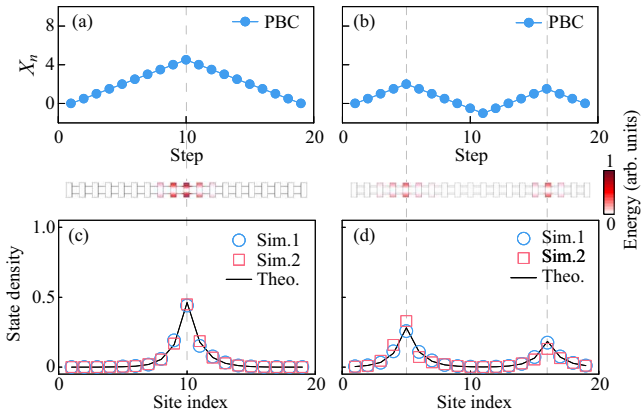

Fig. 4. Programmable acoustic localization in engineered short lattices. (a), (b) The spatial profile of the cumulative parameter X_n, featuring a single prominent peak (a) and two prominent peaks (b). (c), (d) For each configuration, the upper panel shows the spatial distribution of the acoustic field energy, and the lower panel shows the spatial intensity distribution. The simulated intensities, represented by blue circles and pink squares, follow the theoretical profile (black line), with the gray dashed guides confirming the alignment of all peak positions. In panels (a)–(d), the system parameters are $N = 19$ and the gauge field configurations are defined by (a), (c) $h_{1-9} = +0.5$, $h_{10-19} = -0.5$; (b), (d) $h_{1-3,11-15} = +0.5$, $h_{4-10,16-19} = -0.5$.

5. Robust against parameter variations

We further examine the robustness of the established localization patterns by introducing strong local perturbations to the gauge field. Starting from the symmetric single-peak configuration in Fig. 4(a), we alter the value of h_9 from $+0.5$ to $+3$, as shown in Figs. 5(a) and 5(c). This perturbation introduces a strong local defect while largely preserving the global condition $\bar{h} \approx 0$. Remarkably, the primary localization center remains unchanged under this disruption, while the sound intensity on its left side is strongly suppressed, as clearly observed in the simulated acoustic energy field of Fig. 5(c). The persistence of localization at the intended site without adverse

effects demonstrates significant robustness against local defects and symmetry breaking.

We then perform a subsequent modification by setting h_{10} from -0.5 to -3 in the perturbed system, as shown in Figs. 5(b) and 5(d). This subsequent adjustment further drives $\overline{h}$ closer to zero. In this case, the energy becomes intensely localized at the central site, evident in the simulation result of Fig. 5(d). Close agreement between the simulated and theoretical intensity profiles validates the effectiveness of this manipulation. This series of controlled alterations underscores the combination of precise programmability and inherent robustness in the ENHSE.

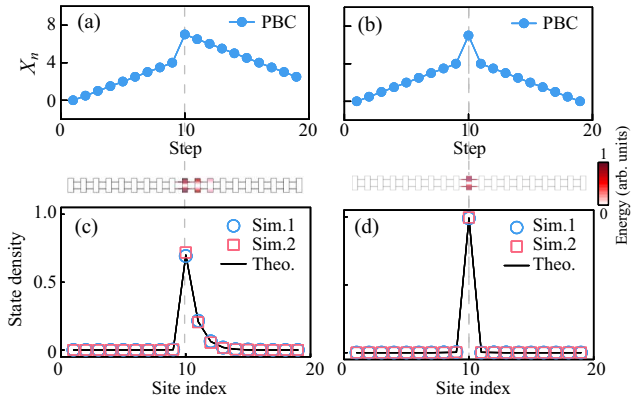

Fig. 5. Robustness of localization under strong gauge field perturbations. (a), (b) The spatial profile of the cumulative parameter X_n, showing the evolution of the peak structure after introducing a local defect at site 9 (a) and a further modification at site 10 (b). (c), (d) Theory–simulation comparison for each case: the upper panel shows the spatial distribution of the acoustic field energy, and the lower panel shows the spatial intensity distribution. The simulated intensities are shown as blue circles (c) and pink squares (d). The gray dashed guides demonstrate the persistence of the primary localization center. All panels are based on the symmetric configuration from Fig. 4(a) with modifications as follows: (a), (c) $h_9 = +3$; (b), (d) $h_9 = +3$, $h_{10} = -3$; all other h_n unchanged.

6. Conclusion

In conclusion, our numerical simulations demonstrate the ENHSE in one-dimensional sonic lattices with disordered non-reciprocal couplings, where acoustic energy localizes at irregular positions throughout the system rather than at boundaries. A key finding is the remarkable correlation between PBC and OBC localization patterns: primary centers persist in both cases, while select PBC peaks collapse into OBC valleys with flanking secondary peaks. We establish that localization sites are quantitatively governed by peaks in the cumulative gauge parameter X_n, derived from the Bernoulli-distributed imaginary gauge field. Importantly, local modifications of this gauge field enable deterministic control over localization — its number, position, and intensity — while maintaining global statistical properties. This programmable energy localization opens pathways for reconfigurable acoustic metamaterials, adaptive energy concentrators, and smart wave processing platforms, establishing a versatile framework for non-Hermitian wave engineering.

Appendix A

The system is described by the tight-binding Hamiltonian

$$\widehat{H} = \sum_{n=1}^{N-1} \left(J_n^{\mathrm{R}} c_{n+1}^{\dagger} c_n + J_n^{\mathrm{L}} c_n^{\dagger} c_{n+1} \right) + \widehat{A}. \tag{A1}$$

Here, N is the system size, $c_n^{\dagger}$ and c_n are the creation and annihilation operators on site n, and $J_n^{\mathrm{R,L}}$ represent the hopping amplitudes to the right (R) and left (L), respectively. The operator $\widehat{A}$ defines the boundary term: $\widehat{A} = 0$ for OBC, and $\widehat{A} = J_N^{\mathrm{R}} c_1^{\dagger} c_N + J_N^{\mathrm{L}} c_N^{\dagger} c_1$ for PBC.

We introduce an imaginary gauge field h_n, where each $h_n = \pm \Delta h$ follows an equal-probability Bernoulli distribution. The hopping amplitudes are defined as

$$J_n^{\mathrm{R}} = J \cdot \exp(h_n), \quad J_n^{\mathrm{L}} = J \cdot \exp(-h_n). \tag{A2}$$

The eigenstates ψ_n and their corresponding eigenvalues E_n satisfy the Schrödinger equation

$$\widehat{H} \psi_n = E \psi_n, \tag{A3}$$

which leads to the following difference equation:

$$E \psi_n = J_{n-1}^{\mathrm{R}} \psi_{n-1} + J_n^{\mathrm{L}} \psi_{n+1} + \widehat{A} \psi_n. \tag{A4}$$

The solutions for OBC and PBC are derived separately below.

Appendix A1. Open boundary conditions

For OBC, where $\widehat{A} = 0$, Eq. (A4) becomes

$$E \psi_n = J_{n-1}^{\mathrm{R}} \psi_{n-1} + J_n^{\mathrm{L}} \psi_{n+1} \tag{A5}$$

for $n = 1, 2, \ldots, N$, with the boundary conditions

$$\psi_0 = \psi_{N+1} = 0. \tag{A6}$$

We introduce a non-unitary gauge transformation

$$\psi_n = \phi_n \exp\left(\sum_{k=1}^{n-1} h_k \right). \tag{A7}$$

Substituting Eqs. (A2) and (A7) into Eq. (A5) yields

$$E \phi_n = J (\phi_{n+1} + \phi_{n-1}). \tag{A8}$$

The boundary conditions for ϕ_n become

$$\phi_0 = \phi_{N+1} = 0. \tag{A9}$$

Assuming a solution of the form $\phi_n = \sin(nq)$ and substituting it into Eq. (A8) gives the eigenvalue

$$E = 2J \cos(q). \tag{A10}$$

Applying the boundary conditions from Eq. (A9), specifically $\phi_{N+1} = \sin[(N+1)q] = 0$, leads to

$$q = \frac{\alpha\pi}{(N+1)},\ \alpha = 1,\ldots,N. \tag{A11}$$

Defining $X_n = \sum_{k=1}^{n-1} h_k$, the final expression for the eigenstates is

$$\psi_n^{(a)} = \sin(nq_a)\exp(X_n), \tag{A12}$$

where $\psi_n^{(a)}$ denotes the n-th component of the a-th eigenstate, and $q_a = a\pi/(N+1)$ denotes the value of q when $\alpha = a$.

Appendix A2. Periodic boundary conditions

For PBC, where $\widehat{A} = J_N^{\mathrm{R}} c_1^\dagger c_N + J_N^{\mathrm{L}} c_N^\dagger c_1$, Eq. (A4) holds for $n = 1,2,\ldots,N$, with the boundary condition

$$\psi_{N+1} = \psi_1. \tag{A13}$$

From Eqs. (A7) and (A13), the boundary condition for ϕ_n is derived as

$$\phi_{N+1} = \phi_1 \exp\left(-\sum_{k=1}^{n} h_k\right) = \phi_1 \exp\left(-N\overline{h}\right), \tag{A14}$$

where $\overline{h} = (1/N)\sum_{k=1}^{N} h_k$ is the mean value of the gauge field.

Assuming a solution of the form $\phi_n = \exp(\mathrm{i}qn - n\overline{h})$ and substituting into the bulk equation derived from Eqs. (A4) and (A2) yields the eigenvalue

$$E = 2J\cos\left(q + \mathrm{i}\overline{h}\right). \tag{A15}$$

A critical insight from Eqs. (A10) and (A15) is that the eigenvalue spectra of the PBC and OBC systems become identical when the average gauge field $\overline{h} = 0$. This condition suppresses the conventional NHSE, thereby facilitating the observation of the ENHSE. Therefore, we consider the case where each $h_n = \pm\Delta h$ takes values of $\pm\Delta h$ with equal probability, following a Bernoulli distribution — a binary probability distribution where each random variable independently assumes one of two possible values with equal likelihood. This setup statistically ensures $\overline{h} \approx 0$, fulfilling the prerequisite for our study of the ENHSE.

Applying the boundary condition Eq. (A14) gives

$$\exp\left[\mathrm{i}q(N+1) - (N+1)\overline{h}\right] = \exp\left(\mathrm{i}q - \overline{h}\right)\cdot\exp\left(-N\overline{h}\right). \tag{A16}$$

Simplifying, we find $\exp(\mathrm{i}qN) = 1$, which leads to the quantization of

$$q = \frac{2\alpha\pi}{N},\ \alpha = 1,2,\ldots,N. \tag{A17}$$

A key condition in this work is $\overline{h} = 0$. Under this condition, the eigenvalue and eigenstate simplify to

$$E = 2J\cos q \tag{A18}$$

$$\psi_n^{(a)} = \exp(\mathrm{i}nq_a)\exp(X_n). \tag{A19}$$

Consider two distinct eigenvalues under PBC:

$$E^{(a)} = 2J\cos\left(\frac{2a\pi}{N+1}\right),\quad E^{(b)} = 2J\cos\left(\frac{2b\pi}{N+1}\right), \tag{A20}$$

where $a,b = 1,2,\ldots,N$ and $a \neq b$. Their corresponding eigenstates are

$$\begin{aligned}\psi_n^{(a)} &= \exp\left(\mathrm{i}\cdot\frac{2na\pi}{N+1}\right)\exp(X_n),\\ \psi_m^{(b)} &= \exp\left(\mathrm{i}\cdot\frac{2mb\pi}{N+1}\right)\exp(X_m)\end{aligned} \tag{A21}$$

for $n,m = 1,2,\ldots,N$, where $\psi_n^{(a)}$ denotes the n-th component of the a-th eigenstate and $\psi_m^{(b)}$ denotes the m-th component of the b-th eigenstate. For the same lattice site ($n = m$), the components of these two eigenstates differ only by a site-independent phase factor $\exp[\mathrm{i}n(b-a)\pi/(N+1)]$, which is a pure imaginary exponent. Consequently, when calculating the spatial density distribution using

$$\text{Probability at site } n = \frac{|\psi_n|^2}{\sum_{k=1}^{N}|\psi_k|^2}, \tag{A22}$$

the phase factors cancel out. Therefore, all eigenstates in the PBC system share the identical spatial density distribution, as the exponential factor $\exp(X_n)$ is common to all.

Appendix B: Experimental methods

To achieve this, the experimental procedure involves: (1) measuring the resonance frequency f_0 of a single cavity and the resonance frequencies f_1 and f_2 of two cavities connected by a waveguide to determine the real coupling strength; (2) characterizing the spatial distribution of coupling strengths across the system, which follows a Bernoulli distribution pattern that we have analyzed using MATLAB; and (3) implementing virtual coupling between adjacent cavities using gain-loss structures to achieve the desired asymmetric coupling strengths $J_n^{\mathrm{R}} = J\exp(h_n)$ and $J_n^{\mathrm{L}} = J\exp(-h_n)$. This is realized by placing speakers in each acoustic cavity to inject phase-shifted acoustic signals from neighboring cavities. Specifically, the gain-loss structures introduce precisely controlled phase shifts to the acoustic signals between adjacent cavities, creating the required non-reciprocal coupling. This method provides a feasible approach to experimentally realizing the desired coupling configuration. Regarding signal quality, noise represents the primary experimental challenge. As discussed in the manuscript, we can selectively enhance specific peaks in the parameter X_n to create strongly localized field concentrations at one or several positions. This approach facilitates clear observation of the erratic non-Hermitian skin effect (ENHSE) in experimental settings.

Appendix C

We have performed the simulation for an $N = 50$ sonic lattice and obtained a representative eigenfield distribution. As shown in Fig. C1, the acoustic energy is not accumulated at the boundaries but at two distinct, irregular positions within the lattice bulk, a hallmark of the ENHSE. The localization strength is uneven between these two sites, with one being significantly more intense. This spatially irregular and multi-focal localization pattern — fundamentally different from the boundary-localized modes in conventional NHSE — serves as a clear numerical signature of ENHSE.

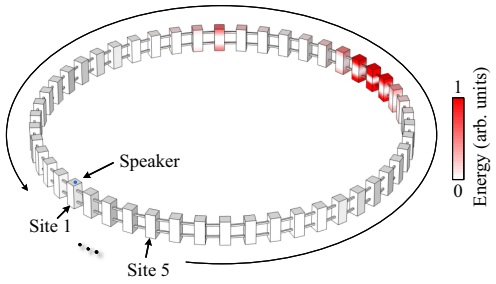

Fig. C1. Schematic of a representative acoustic field distribution in an $N = 50$ sonic lattice exhibiting ENHSE characteristics.

Data availability statement

Additional information is available from the corresponding authors upon request.

Acknowledgments

This work was supported by the National Natural Science Foundation of China (Grant No. 12404504) and Jiangsu Provincial Natural Science Foundation (Grant No. BK20231031).

References

[1] Hatano N and Nelson D R 1996 *Phys. Rev. Lett.* **77** 570
[2] Hatano N and Nelson D R 1998 *Phys. Rev. B* **58** 8384
[3] Mostafazadeh A 2002 *J. Math. Phys.* **43** 205
[4] Bender C M and Boettcher S 1998 *Phys. Rev. Lett.* **80** 5243
[5] Hu Y C and Hughes T L 2011 *Phys. Rev. B* **84** 153101
[6] Liang S D 2013 *Phys. Rev. A* **87** 012118
[7] Ashida Y, Gong Z and Ueda M 2020 *Adv. Phys.* **69** 249
[8] Chen W, Özdemir S K, Zhao G and Yang Y 2017 *Nature* **548** 192
[9] Ding K, Fang C and Ma G 2022 *Nat. Rev. Phys.* **4** 745
[10] Wang Z, Liang Z, Hu J, Zhou P, Liu L, Hu G, Wang W and Ye M 2025 *Adv. Quantum Technol.* **8** 2400349
[11] Feng L, El-Ganainy R and Ge L 2017 *Nat. Photonics* **11** 752
[12] Hu B, Zhang Z, Zhang H, Zheng L, Xiong W, Yue Z, Wang X, Xu J, Cheng Y, Liu X and Christensen J 2021 *Nature* **597** 655
[13] Delplace P, Yoshida T and Hatsugai Y 2021 *Phys. Rev. Lett.* **127** 186602
[14] Zhang H, Hu B, Xiong W, Cheng Y and Liu X 2023 *Sci. China-Phys. Mech. Astron.* **66** 124312
[15] Hu B, Zhang Z, Yue Z, Liao D, Liu Y, Zhang H, Cheng Y, Liu X and Christensen J 2023 *Phys. Rev. Lett.* **131** 066601
[16] Bergman A, Duggan R, Sharma K, *et al*. 2021 *Nat. Commun.* **12** 486
[17] Rao Z, Meng C, Han Y, *et al*. 2024 *Nat. Phys.* **20** 1904
[18] Xiao L, Deng T, Wang K, *et al*. 2020 *Nat. Phys.* **16** 761
[19] Hu Y M, Huang Y Q, Xue W T and Wang Z 2024 *Phys. Rev. B* **110** 205429
[20] Hu H and Zhao E 2021 *Phys. Rev. Lett.* **126** 010401
[21] Zou D, Chen T, He W, *et al*. 2021 *Nat. Commun.* **12** 7201
[22] Zhang X, Tian Y, Jiang J H, *et al*. 2021 *Nat. Commun.* **12** 5377
[23] Hou W, Tang H, Xu Q and Lin Y 2024 *Chin. Phys. Lett.* **41** 040301
[24] Lee C H, Li L and Gong J 2019 *Phys. Rev. Lett.* **123** 016805
[25] Okuma N, Kawabata K, Shiozaki K and Sato M 2020 *Phys. Rev. Lett.* **124** 086801
[26] Zhang L, Yang Y, Ge Y, *et al*. 2021 *Nat. Commun.* **12** 6297
[27] Xiao Y X and Chan C T 2022 *Phys. Rev. B* **105** 075128
[28] Zhang K, Shu C and Sun K 2025 *Phys. Rev. X* **15** 031039
[29] Wang Y A and Li L 2025 *Chin. Phys. Lett.* **42** 037301
[30] Li L, Lee C H, Mu S, *et al*. 2020 *Nat. Commun.* **11** 5491
[31] Wang W, Wang X and Ma G 2022 *Nature* **608** 50
[32] Rosa M I N and Ruzzene M 2020 *New J. Phys.* **22** 053004
[33] Xiao L, Xue W T, Song F, Hu Y M, Yi W, Wang Z and Xue P 2024 *Phys. Rev. Lett.* **133** 070801
[34] Lin Z, Song W, Wang L W, Xin H, Sun J, Wu S, Huang C, Zhu S, Jiang J H, *et al*. 2024 *Phys. Rev. Lett.* **133** 073803
[35] Huang Q K L, Liu Y K, Cao P C, Zhu X F and Li Y 2023 *Chin. Phys. Lett.* **40** 106601
[36] Claes J and Hughes T L 2021 *Phys. Rev. B* **103** L140201
[37] Zhang Z Q, Liu H, Liu H, Jiang H and Xie X C 2023 *Sci. Bull.* **68** 157
[38] Liu H, Lu M, Zhang Z Q and Jiang H 2023 *Phys. Rev. B* **107** 144204
[39] Longhi S 2025 *Phys. Rev. Lett.* **134** 196302